PCCP

Natural reaction orbitals for characterizing electron transfer responsive to nuclear coordinate displacement

Journal:	*Physical Chemistry Chemical Physics*
Manuscript ID	CP-ART-09-2021-004491.R1
Article Type:	Paper
Date Submitted by the Author:	24-Oct-2021
Complete List of Authors:	Ebisawa, Shuichi; Hokkaido Univ Hasebe, Masatoshi; Hokkaido Univ Tsutsumi, Takuro; Hokkaido Univ, Department of Chemistry, Faculty of Science Tsuneda, Takao; Kobe University, Taketsugu, Tetsuya; Hokkaido Univ, Department of Chemistry, Faculty of Science

Natural reaction orbitals for characterizing electron transfer responsive to nuclear coordinate displacement

Shuichi Ebisawa[1], Masatoshi Hasebe[1], Takuro Tsutsumi[2], Takao Tsuneda[2,3],

Tetsuya Taketsugu[2,4 *]

1 Graduate School of Chemical Sciences and Engineering, Hokkaido University, Sapporo 060-0810, Japan
2 Department of Chemistry, Faculty of Science, Hokkaido University, Sapporo 060-0810, Japan
3 Graduate School of Science Technology and Innovation, Kobe University, Nada-ku, Kobe, Hyogo 657-8501, Japan
4 Institute for Chemical Reaction Design and Discovery (WPI-ICReDD), Hokkaido University, Sapporo 001-0021, Japan

Abstract

Natural reaction orbital (NRO) is proposed as a new concept for analyzing chemical reactions from the viewpoint of the electronic theory. The pair of the occupied and virtual NROs that characterize electron transfer responsive to nuclear coordinate displacement along the reaction path is automatically extracted from the solution of the coupled-perturbed self-consistent-field (CPSCF) equation for the perturbation of the nuclear displacement. The NRO-based reaction analysis method is applied to several reactions. As a result, it is found that the sum of squares of the singular values, derived from the solution of the CPSCF equation, gives sharp peaks around the transition state structures and at the shoulders of the potential energy curve. The peaks around the transition states suggest a new physical meaning of transition state from the viewpoint of the electronic theory. Furthermore, the double peaks reveal the asynchronous processes of reactions, which are not always shown in potential energy analyses. Since the NRO-based reaction analysis method is universal and robust for describing reaction mechanisms from an electronic theory viewpoint, it is expected to lead to universal reaction analyses based on the electronic theory.

I. Introduction

Molecular orbitals (MOs) are gaining in importance both experimentally and theoretically. In experimental studies, the phases of MOs have been observed by multidimensional electron spectroscopy and MO tomography. Multidimensional electron spectroscopy provides MO patterns by measuring the binding energies for removing electrons from MOs by various means as well as by evaluating new physical quantities as parameters.[1–3] On the other hand, MO tomography has recently attracted much attention as a versatile experimental technique to draw MO images by computed tomography scanning of molecules using an intense photon laser.[4,5] These methods allow us to observe not only the HOMO but also a certain number of occupied and unoccupied valence orbitals. Therefore, tracking chemical reactions based on MOs has been experimentally realized. On the other hand, theoretical studies have been able to provide quantitative MO energies. The occupied and unoccupied orbital energies are established to be identical to the minus signs of the corresponding ionization potential and electron affinity, respectively.[6] It has been proven that the long-range corrected density functional theory (DFT)[7] accurately reproduces the valence orbital energy by satisfying the Sham-Schlüter theorem[8] with respect to the orbital energy quite well.[9] This progress in experimental and theoretical MO study has raised expectations for chemical reaction analysis based on MOs.

Reaction orbital theory is a theory developed to analyze reactions based on MOs. A representative reaction orbital theory is the frontier orbital (FO) theory,[10,11] which forms the basis of the Woodward-Hoffmann rule[12–16] for pericyclic reactions and has led to the development of various reaction orbital theories, including the conceptual DFT[17] and reactive orbital energy theory.[18,19] MOs are usually obtained as the eigenfunctions of one-electron self-consistent field (SCF) equations such as the Hartree-Fock equation and the Kohn-Sham equation. However, such conventional MOs, which we call "*canonical MOs (CMOs)*," have two drawbacks in the analysis of reaction mechanisms based on reaction orbital theory:

1. Virtual CMOs are usually too delocalized to be analyzed especially in high-quality calculations using diffuse basis functions, although the orbital shapes and the interactions between occupied and virtual orbitals are essentially needed to explain the reactivity of molecular systems in reaction orbital theory.
2. It is difficult to find the MOs that activate the reaction because there are too many CMOs to make a clear analysis, even if it is limited to valence CMOs of relatively small molecules.

Various concepts of MOs have been developed to solve these difficulties of CMO. Recently, Krylov[20] has claimed that the definition of the optimal MO is not uniquely determined. More precisely, it is argued that it is appropriate to define MOs

in relation to the relevant observables, rather than sticking to a single definition. Indeed, a variety of orbital definitions have been successfully applied to the analysis of specific chemical properties and events. Natural bond orbital (NBO)[21,22] analysis has been used to interpret chemical bond structures in the electronic wavefunction of a given geometrical structure. The intrinsic soft MO (ISMO) method[23] transforms the CMO by singular value decomposition (SVD) on the U matrix obtained as a solution to the coupled-perturbed SCF (CPSCF) equation[24–28] to identify the MOs that are important for the response of electrons to the distortion of the external electrostatic field. Natural transition orbital (NTO)[29] analysis is a technique to extract pairs of occupied and virtual orbitals that characterize an excited state using the SVD of the one-electron transition density matrix. The recently proposed principal interacting orbital (PIO) method[30–32] also uses the SVD technique to analyze the density matrix in terms of interacting fragments of a molecular system. Although analyses based on these orbitals are very useful for exploring chemical bonding and chemical phenomena in terms of electronic wavefunctions, no approach has explicitly taken into account the nuclear displacement associated with chemical reactions. Considering Krylov's argument, MOs for discussing chemical reactions should be defined in relation to quantities that characterize the electronic wavefunction variation along the reaction coordinate.

We propose an orbital-based reaction analysis method that generates occupied-virtual orbital pairs that characterize the electron density change along the reaction path by applying SVD to the U matrix of the CPSCF equation. The generated pair of occupied and virtual orbitals is named "*natural reaction orbital (NRO)*." As shown in this paper, NRO improves the above two problems of CMO and enables us to automatically extract reactive orbital pairs essential for chemical reactions without relying on chemical intuition. In the past, many efforts have been made to extract such reactive orbitals, some of which require empirical intuition and in-depth knowledge other than the calculation results, and the process is time-consuming. Thus, the reaction analysis method using NRO is expected to prevent misunderstandings due to misinterpretation of calculation results and human errors in determining reactive orbitals.

This method has been applied to several representative reactions: e.g., the electron transfer reaction between the formaldehyde anion (H_2CO^-) and methyl chloride (CH_3Cl), which is known to have a post-transition-state bifurcation.[33–37] In Sec. II, we briefly describe the CPSCF equation and then introduce the generation of NRO. Sec. III presents applications of NROs to several reactions in order to validate their effectiveness. Sec. IV summarizes the significance of NROs and discusses their future prospects.

II. Method for generating natural reaction orbitals

In this section, we describe the procedure for generating *natural reaction orbitals (NROs)* based on the U matrix, which is the solution to the CPSCF equation. Henceforth, the subscripts $i\ (i = 1, \dots, N_{\mathrm{occ}})$, $a\ (a = N_{\mathrm{occ}} + 1, \dots, N_{\mathrm{occ}} + N_{\mathrm{vir}})$, and $p\ (p = 1, \dots, N_{\mathrm{occ}} + N_{\mathrm{vir}})$ are used for occupied, virtual, and all spin orbitals, respectively, and the subscripts μ and ν are used for atomic orbitals (AO).

First, the CPSCF equation[24–28] is briefly reviewed. The Hartree-Fock-Roothaan (HFR) equation is represented as

$$\mathbf{F}(0)\mathbf{C}(0) = \mathbf{S}(0)\mathbf{C}(0)\mathbf{E}(0), \quad (1)$$

where $\mathbf{F}, \mathbf{C}, \mathbf{S}$, and $\mathbf{E}$ are the Fock matrix, the MO coefficient matrix, the overlap matrix, and the diagonal orbital energy matrix, respectively, and 0 denotes the unperturbed nuclear coordinates. For a perturbed geometric structure shifted by an infinitesimal displacement parameter $\tau(>0)$ in the direction of the unit vector $\boldsymbol{n}$, the HFR equation is given by

$$\mathbf{F}(\tau)\mathbf{C}(\tau) = \mathbf{S}(\tau)\mathbf{C}(\tau)\mathbf{E}(\tau). \quad (2)$$

By expanding the respective matrices in Eq. (2) by powers of τ as

$$\begin{aligned} \mathbf{F}(\tau) &= \mathbf{F}(0) + \tau\mathbf{F}^{(1)}(0) + O(\tau^2), \\ \mathbf{C}(\tau) &= \mathbf{C}(0) + \tau\mathbf{C}^{(1)}(0) + O(\tau^2), \\ \mathbf{S}(\tau) &= \mathbf{S}(0) + \tau\mathbf{S}^{(1)}(0) + O(\tau^2), \\ \mathbf{E}(\tau) &= \mathbf{E}(0) + \tau\mathbf{E}^{(1)}(0) + O(\tau^2), \end{aligned} \quad (3)$$

and equating the first-order terms, we get

$$\mathbf{F}^{(1)}(0)\mathbf{C}(0) + \mathbf{F}(0)\mathbf{C}^{(1)}(0) = \mathbf{S}^{(1)}(0)\mathbf{C}(0)\mathbf{E}(0) + \mathbf{S}(0)\mathbf{C}^{(1)}(0)\mathbf{E}(0) + \mathbf{S}(0)\mathbf{C}(0)\mathbf{E}^{(1)}(0). \quad (4)$$

Note that these first-order responses depend on the direction of $\boldsymbol{n}$. Henceforth, since Eq. (4) is given in the τ-free form, we omit the 0 representing the nuclear coordinates. Multiplying both sides of Eq. (4) by $\mathbf{C}^{\dagger}$, the Hermitian conjugate of $\mathbf{C}$ from the left, and using Eq. (1), we obtain the following equation as

$$\mathbf{C}^{\dagger}\mathbf{F}^{(1)}\mathbf{C} + \mathbf{E}\mathbf{C}^{\dagger}\mathbf{S}\mathbf{C}^{(1)} = \mathbf{C}^{\dagger}\mathbf{S}^{(1)}\mathbf{C}\mathbf{E} + \mathbf{C}^{\dagger}\mathbf{S}\mathbf{C}^{(1)}\mathbf{E} + \mathbf{E}^{(1)}. \quad (5)$$

Introducing the matrices of $\tilde{\mathbf{F}}^{(1)}$, $\mathbf{U}^{(1)}$ and $\tilde{\mathbf{S}}^{(1)}$ in the form of

$$\begin{aligned} \tilde{\mathbf{F}}^{(1)} &= \mathbf{C}^{\dagger}\mathbf{F}^{(1)}\mathbf{C}, \\ \mathbf{U}^{(1)} &= \mathbf{C}^{\dagger}\mathbf{S}\mathbf{C}^{(1)}, \\ \tilde{\mathbf{S}}^{(1)} &= \mathbf{C}^{\dagger}\mathbf{S}^{(1)}\mathbf{C}, \end{aligned} \quad (6)$$

Eq. (5) is rewritten as

$$\mathbf{E}\mathbf{U}^{(1)} - \mathbf{U}^{(1)}\mathbf{E} = \tilde{\mathbf{S}}^{(1)}\mathbf{E} - \tilde{\mathbf{F}}^{(1)} + \mathbf{E}^{(1)}. \quad (7)$$

The first-order orthonormality condition for MOs is expressed as

$$\mathbf{U}^{(1)\dagger} + \tilde{\mathbf{S}}^{(1)} + \mathbf{U}^{(1)} = \mathbf{0}. \quad (8)$$

Solving Eqs. (7) and (8) yields $\mathbf{E}^{(1)}$ and the virtual-occupied block of $\mathbf{U}^{(1)}$. The equation to obtain the virtual-occupied block of $\mathbf{U}^{(1)}$ as

$$(\epsilon_a - \epsilon_i)\mathrm{U}_{ai}^{(1)} = \epsilon_i \tilde{\mathrm{S}}_{ai}^{(1)} - \tilde{\mathrm{F}}_{ai}^{(1)} \quad (9)$$

is called coupled perturbed Hartree-Fock (CPHF) equation where ϵ_i and ϵ_a are occupied and virtual orbital energies, respectively. The coupled perturbed Kohn-Sham (CPKS) equation is obtained by replacing the Fock matrix with an effective Hamiltonian matrix for the Kohn-Sham equation. For the details of the CPHF and CPKS equations, see Refs. 24–28.

Let us introduce the operator transforming the unperturbed occupied CMOs to the perturbed ones,

$$\mathcal{T}(\tau,0) = \sum_{p=1}^{N_{\mathrm{occ}}+N_{\mathrm{vir}}} n_p |\psi_p(\tau)\rangle\langle\psi_p(0)| = \sum_{i=1}^{N_{\mathrm{occ}}} \sum_{\mu,\nu} c_{\mu i}(\tau) c_{\nu i}^*(0) |\chi_\mu(\tau)\rangle\langle\chi_\nu(0)|, \quad (10)$$

where n_p is the occupation number of the p-th spin orbital (*i.e.* $n_i = 1$ and $n_a = 0$), ψ_p and χ_μ are the p-th CMO and μ-th AO, respectively, and τ is the infinitesimal nuclear displacement parameter. Expanding $c_{\mu i}(\tau)$ by powers of τ gives the zeroth- and first-order transformation operators,

$$\mathcal{T}^{(0)}(\tau,0) = \sum_{i=1}^{N_{\mathrm{occ}}} \sum_{\mu,\nu} c_{\mu i}(0) c_{\nu i}^*(0) |\chi_\mu(\tau)\rangle\langle\chi_\nu(0)|, \quad (11)$$

$$\mathcal{T}^{(1)}(\tau,0) = \sum_{p=1}^{N_{\mathrm{occ}}+N_{\mathrm{vir}}} \sum_{i=1}^{N_{\mathrm{occ}}} \sum_{\mu,\nu} c_{\mu p}(0) \mathrm{U}_{pi}^{(1)}(0) c_{\nu i}^*(0) |\chi_\mu(\tau)\rangle\langle\chi_\nu(0)|, \quad (12)$$

where we used the definition of $\mathbf{U}^{(1)}$ as

$$\mathbf{C}^{(1)}(0) = \mathbf{C}(0)\mathbf{U}^{(1)}(0). \quad (13)$$

The zeroth-order operator works only to translate the AOs without mixing the CMOs, while the first-order operator causes mixing of CMOs as the AOs are translated. Actually, the translation of AOs and the mixing of CMOs can be separated as follows

$$\mathcal{T}^{(1)}(\tau,0) = \mathcal{T}^{(0)}(\tau,0)\mathcal{U}^{(1)}(0), \quad (14)$$

where the first-order mixing operator $\mathcal{U}^{(1)}(0)$ is defined as

$$\mathcal{U}^{(1)}(0) = \sum_{p=1}^{N_{\mathrm{occ}}+N_{\mathrm{vir}}} \sum_{i=1}^{N_{\mathrm{occ}}} \sum_{\mu,\nu} c_{\mu p}(0) \mathrm{U}_{pi}^{(1)}(0) c_{\nu i}^*(0) |\chi_\mu(0)\rangle\langle\chi_\nu(0)| = \sum_{p=1}^{N_{\mathrm{occ}}+N_{\mathrm{vir}}} \sum_{i=1}^{N_{\mathrm{occ}}} \mathrm{U}_{pi}^{(1)}(0) |\psi_p(0)\rangle\langle\psi_i(0)|. \quad (15)$$

The occupied-occupied terms are a rather trivial part of the mixing because the Slater determinant is invariant under the first-order mixing between occupied orbitals. Accordingly, we define the first-order one-electron transition density operator as

$$\mathcal{U}_{\mathrm{VO}}^{(1)}(0) = \sum_{a=N_{\mathrm{occ}}+1}^{N_{\mathrm{occ}}+N_{\mathrm{vir}}} \sum_{i=1}^{N_{\mathrm{occ}}} \mathrm{U}_{ai}^{(1)}(0)|\psi_a(0)\rangle\langle\psi_i(0)|. \quad (16)$$

$\mathcal{U}_{\mathrm{VO}}^{(1)}(0)$ is expanded with the basis functions in the unperturbed geometry. Consequently, the mixing between CMOs along the nuclear displacement can be analyzed in terms of the basis function in the unperturbed geometry. The singular value decomposition (SVD) of $\mathbf{U}_{\mathrm{VO}}^{(1)}(0)$ yields the $N_{\mathrm{occ}} \times N_{\mathrm{occ}}$ unitary matrix $\mathbf{O}$ and the $N_{\mathrm{vir}} \times N_{\mathrm{vir}}$ unitary matrix $\mathbf{V}$ as

$$\mathbf{U}_{\mathrm{VO}}^{(1)}(0) = \mathbf{V}\boldsymbol{\Lambda}\mathbf{O}^{\dagger}, \quad (17)$$

where $\boldsymbol{\Lambda}$ is a rectangular diagonal matrix of size $N_{\mathrm{vir}} \times N_{\mathrm{occ}}$. The non-negative real numbers in the diagonal part of $\boldsymbol{\Lambda}$, λ_i $(i = 1, \dots, N_{\mathrm{occ}})$, are called the singular values of $\mathbf{U}^{(1)}(0)$. The occupied and virtual CMOs are transformed by the unitary matrix $\mathbf{O}$ and the unitary matrix $\mathbf{V}$, respectively, as follows:

$$\left(\phi_1, \phi_2, \dots, \phi_{N_{\mathrm{occ}}}\right) = \left(\psi_1, \psi_2, \dots, \psi_{N_{\mathrm{occ}}}\right)\mathbf{O}, \quad (18)$$

$$\left(\phi'_1, \phi'_2, \dots, \phi'_{N_{\mathrm{vir}}}\right) = \left(\psi_{N_{\mathrm{occ}}+1}, \psi_{N_{\mathrm{occ}}+2}, \dots, \psi_{N_{\mathrm{occ}}+N_{\mathrm{vir}}}\right)\mathbf{V}. \quad (19)$$

The set of orbitals in Eqs. (18) and (19), *i.e.*, $\left(\phi_1, \phi_2, \dots, \phi_{N_{\mathrm{occ}}}\right)$ and $\left(\phi'_1, \phi'_2, \dots, \phi'_{N_{\mathrm{vir}}}\right)$, are named as *natural reaction orbitals (NROs)*. Henceforth, virtual NROs will be marked with the prime symbol to avoid any misunderstanding. Singular values, λ_i, are assigned to N_{occ} pairs of occupied NROs and virtual NROs: ϕ_i and ϕ'_i (where we assume $N_{\mathrm{occ}} \leq N_{\mathrm{vir}}$). All the singular values for the rest of the virtual NROs are zero, *i.e.* $\lambda_a = 0$ $(a > N_{\mathrm{occ}})$.

Now consider the physical meaning of the singular value for the pair of occupied and virtual NROs. As shown in Eq. (14), the first-order orbital responses can be divided into mixing of orbitals in the unperturbed structure and subsequent translation of the AOs. The virtual-occupied orbital mixing changes the *i*-th NRO as

$$\phi_i(0) \rightarrow \phi_i(0) + \tau\lambda_i\phi'_i(0) \quad (i = 1, \dots, N_{\mathrm{occ}}), \quad (20)$$

where τ is the infinitesimal displacement parameter. This relation indicates that the virtual NRO mixes with the occupied NRO under the perturbation of nuclear coordinate displacement, and the corresponding singular value evaluates its mixing rate. Therefore, the occupied-virtual NRO pairs with large singular values are more correlated with nuclear coordinate displacement than those with small singular values.

There are two important properties of NROs. First, the relative phases of NRO pairs with non-zero singular values

are uniquely determined for a given nuclear displacement direction. If we reverse the sign of the *i*-th column (*i*-th occupied NRO coefficient) of $\mathbf{O}^{\dagger}$ in Eq. (17), we must also reverse the sign of the *i*-th row (*i*-th virtual NRO coefficient) of $\mathbf{V}$ in order for the equation to hold. Second, when the direction of nuclear displacement is reversed, the relative phase of each NRO pair is also reversed. This comes from the fact that the sign of $\mathbf{U}_{\mathrm{VO}}^{(1)}(0)$ is reversed when the direction of nuclear displacement is reversed. In the next section, we will discuss these two points again when applying NRO analysis to specific chemical reactions.

As for the computational cost, the bottleneck for determining NROs is the step of solving the CPSCF equation to obtain the U matrix for a given structure.[38] In the commonly used quantum chemical calculation program packages, the CPSCF equation is solved to calculate the analytic Hessian matrix, so the U matrix data can be obtained by performing normal mode analysis. However, NRO analysis does not require the U matrix for displacements in the direction of all degrees of freedom of the nucleus, but only the U matrix for displacements in the reaction coordinate direction. If the CPSCF equation cannot be solved analytically, the U matrix can be obtained by numerical differentiation like $\mathbf{U}^{(1)} \sim (2\tau)^{-1}\mathbf{C}^{\dagger}(0)\mathbf{S}(0)\big(\mathbf{C}(\tau) - \mathbf{C}(-\tau)\big)$.

Note that the applicability of the NRO method is limited to the electronic structure theories for single electron configurations, e.g., the HFR and KS SCF methods, in the present form, though there are many chemical reactions involving explicit bond dissociation/formation processes that require multiconfiguration wave functions to be reproduced. The inapplicability of the NRO method to such multiconfigurational reactions remains to be solved for comprehensively investigating chemical reactions. Methods such as the Electron Localization Index (ELI)[39,40] are useful for the analysis of electronic structure changes based on multi-configuration wave function theory. However, we would emphasize that chemical reactions of single-configurational nature are the majority, and the NRO method is a powerful tool for discussing the reaction paths of major reactions.

Finally, we would like to comment on the difference between the NRO method and the ISMO method.[23] The ISMO method also transforms the CMO by applying SVD to the virtual-occupied term of $\mathbf{U}^{(1)}$ obtained from the CPSCF equation, but the perturbation is not a displacement of the nuclear coordinates but a fluctuation of the partial charges. In the viewpoint of solvent effects, ISMOs with large singular values are particularly important for the response of electrons to surrounding solvent molecules. On the other hand, NRO is concerned with electron transfer and bond rearrangement in chemical reaction

processes, as seen in organic electron theory. In other words, NRO clarifies the mechanism of electron transfer from occupied orbital space to virtual orbital space when the structure changes along the reaction path, which is useful for understanding the reaction mechanism based on the orbital picture.

III. Results and discussion

In this section, we examine the NRO method for six typical reactions in order to prove the applicability. Different calculation methods and basis sets are used for the NRO analyses of these reactions to check the availability of the NRO method. In the case of the comparative discussions to previous related studies, we, however, use the same computational levels as those in the previous studies.

A. Electron transfer reaction between formaldehyde anion and methyl chloride

First, NRO analysis is applied to the electron transfer reaction between the formaldehyde anion and methyl chloride to demonstrate that NRO can be a powerful tool for understanding the characteristics of electron transfer in reactions. As shown in **Fig. 1**, this reaction is known to exhibit a post-transition-state bifurcation: the reactant cluster (C_R) is transformed into either the C-alkylation cluster ($C_{SUB(C)}$) or the dissociative electron transfer cluster (C_{ET}) through the common electron transfer transition state (ET-TS).[33–37] For this reaction, the features of electron transfer have been investigated using a valence bond configuration mixing (VBCM) analysis.[33–36] This reaction is, therefore, suitable to test the performance of the NRO analysis. We, therefore, apply the NROs to the intrinsic reaction coordinate (IRC)[41] from C_R to $C_{SUB(C)}$ through the ET-TS with keeping the C_s point group symmetry. The structure optimization of ET-TS and the calculations of IRC and the $U_{ai}^{(1)}$ were carried out for the doublet ground state by spin-unrestricted Hartree-Fock (UHF) with the 6-31+G(d,p) basis set.[42–45] All the calculations were performed using Gaussian16 Rev.C.01.[46]

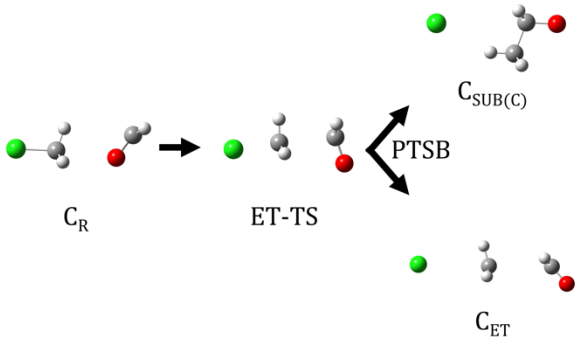

Figure 1. Schematic picture of the post-transition-state bifurcation (PTSB) in the electron transfer reaction of formaldehyde anion (H_2CO^-) and methyl chloride (CH_3Cl): the reactant cluster (C_R) changes to the C-alkylation cluster $C_{SUB(C)}$ or the dissociative electron transfer cluster C_{ET} through the electron transfer transition state (ET-TS). The IRC from ET-TS to the product side leads to $C_{SUB(C)}$.

Let us focus on the MOs at the ET-TS structure, assuming that the electron transfer proceeds associated with bond formation and dissociation near the TS structure. **Figure 2** illustrates the valence CMOs for the HOMO−4 to LUMO+4 of α- and β-spin electrons at the ET-TS structure. Note that the HOMO of β-spin corresponds to the HOMO-1 of α-spin, because the spin multiplicity is a doublet. As shown in this figure, the electronic distribution of the virtual CMOs tends to be too delocalized to discuss the electron transfer between the occupied CMOs and the virtual CMOs.

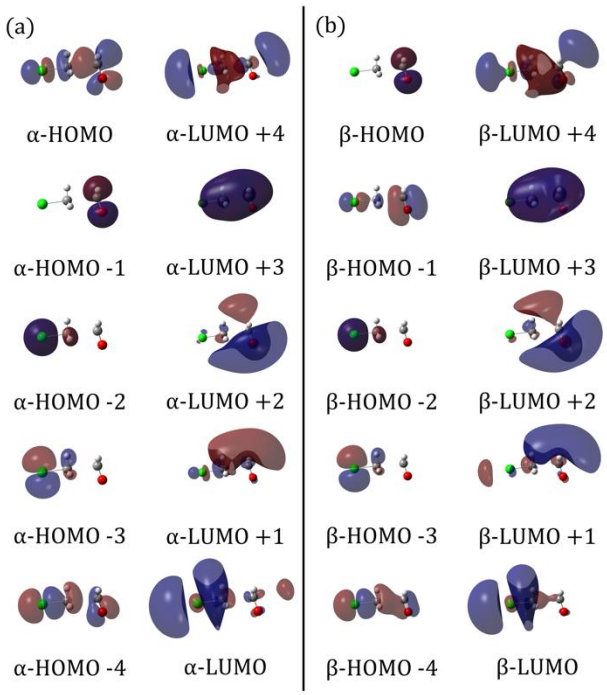

Figure 2. Five occupied and five virtual valence CMOs at the ET-TS for (a) α- and (b) β-spin electrons with the isovalue of 0.02.

Figure 3 displays the square of the singular values of the $\mathbf{U}_{\mathrm{VO}}^{(1)}$ matrix in Eq. (17) for the α- and β-spin orbitals with the NRO pairs of the maximum singular values (ϕ_1^{α} and $\phi_1'^{\alpha}$) at the ET-TS structure, for the nuclear displacements along the IRC following the mode with the imaginary frequency at the transition state (**Fig. 4**). The singular value indicates the mixing level of the occupied and virtual NROs following the nuclear displacement. For the pair of ϕ_1^{α} and $\phi_1'^{\alpha}$, the singular value is λ_1^{α} = 0.362 amu$^{-1/2}$ bohr^{-1}, which accounts for the 94.8% of the α-spin occupied-virtual orbital mixing, indicating that the NRO pair ϕ_1^{α} and $\phi_1'^{\alpha}$ fully explains the electron transfer in this reaction. The results show that the NROs solve

the difficulty in the analyses coming from the highly-delocalized virtual CMOs. The sum of the squared singular values of the β-spin orbitals, $\| \mathbf{\Lambda}^{\beta} \|_F^2$ (= 0.020 amu^{-1} bohr^{-2}) is much smaller than that of the α-spin orbitals, $\| \mathbf{\Lambda}^{\alpha} \|_F^2$ (= 0.138 amu^{-1} bohr^{-2}). Note that this NRO analysis hardly depends on the basis set used, because almost the same NRO shapes and major NRO contributions are obtained for the 6-31+G(d,p) and aug-cc-pVTZ basis sets,[47–49] as shown in **Fig. 5**. This robustness supports the reliability of NRO-based analyses.

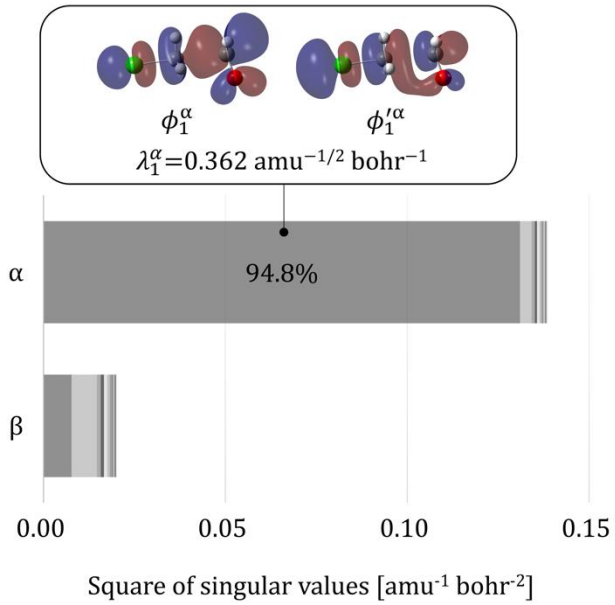

Figure 3. Distribution of squared singular values of $\mathbf{U}_{\mathrm{VO}}^{(1)}$ for α- and β-spin NROs associated with nuclear displacements along the imaginary frequency mode at the ET-TS structure of the H_2CO^- + CH_3Cl reaction. The major NRO pairs corresponding to the largest singular values are also shown.

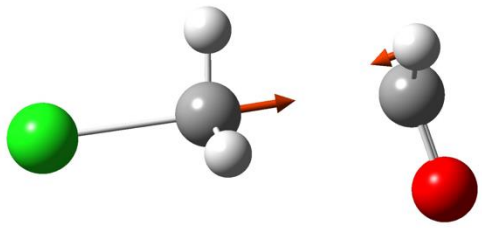

Figure 4. Imaginary frequency mode at the ET-TS structure of H_2CO^- + CH_3Cl reaction.

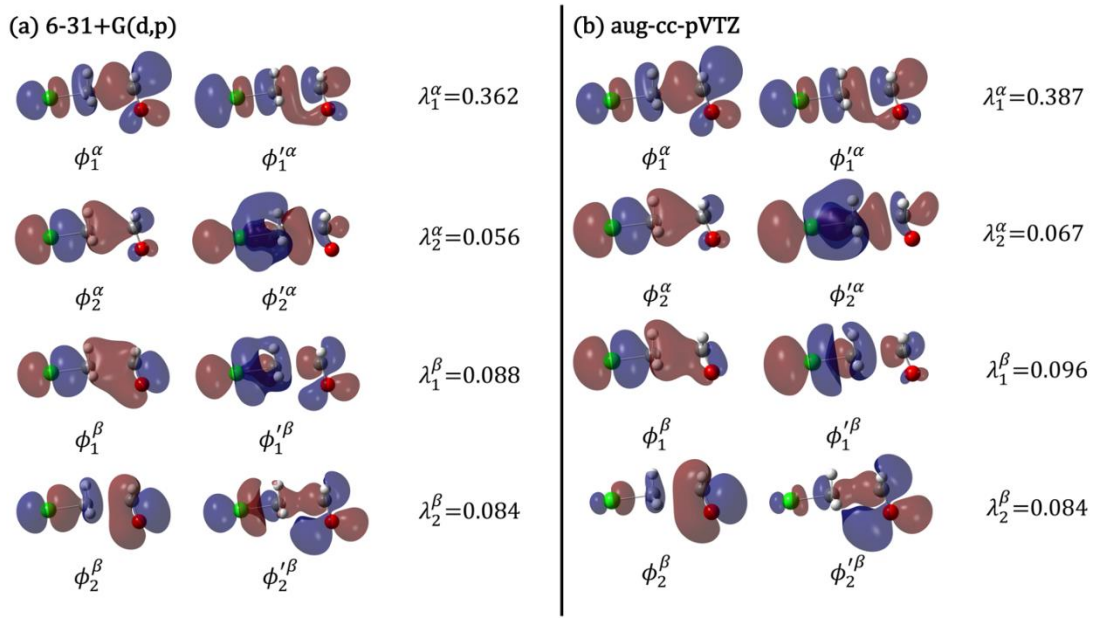

Figure 5. NROs at the ET-TS of H_2CO^- + CH_3Cl reaction with the imaginary frequency mode for the nuclear displacement direction toward the product by the UHF calculations with (a) 6-31+G(d,p) and (b) aug-cc-pVTZ basis sets. The occupied and virtual NROs of the maximum and second maximum singular values are also shown for α- and β-spin orbitals.

As shown in **Fig. 5**, the occupied NRO, ϕ_1^α, transforms into $\phi_1^\alpha + 0.362\tau\phi_1'^\alpha$ due to the virtual-occupied mixing caused by the nuclear displacement along the reaction coordinate toward the product. This transformation decreases the electron density of formaldehyde due to the mixing of ϕ_1^α and $\phi_1'^\alpha$ in the opposite-sign phases, while increasing the electron density of methyl chloride due to the mixing of ϕ_1^α and $\phi_1'^\alpha$ in the same-sign phases (**Fig. 6**). As a result, the electron transfers from the formaldehyde anion to methyl chloride. The opposite process toward the reactant makes progress as $\phi_1^\alpha \rightarrow \phi_1^\alpha - 0.362\tau\phi_1'^\alpha$. For the opposite direction of nuclear displacement, the relative phase of each NRO pair is reversed to give the minus sign of $\phi_1'^\alpha$, as discussed in Sec. II. Therefore, the electron transfers from methyl chloride to formaldehyde anion.

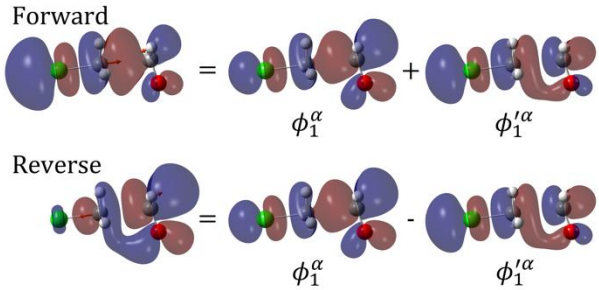

Figure 6. Orbital mixing of occupied and virtual NRO pairs (ϕ_1^α and $\phi_1'^\alpha$) with the maximum singular value for nuclear displacements in the directions toward the product (forward) and the reactant (reverse) along the imaginary frequency mode at the ET-TS of the H_2CO^- + CH_3Cl reaction.

Note that NROs can be classified by the irreducible representations of the point group in the molecular structure. For the H_2CO^- + CH_3Cl reaction, the reaction complex has C_s point group symmetry at the ET-TS structure and the imaginary frequency mode belongs to the A' irreducible representation, while any NRO belongs to either A' or A'' representation. Similar to the selection rule of electronic excitations for giving non-zero transition amplitudes, the direct product of the irreducible representations of the occupied NRO, virtual NRO, and nuclear displacements must be totally symmetric. Therefore, the occupied and virtual NROs in the same pair belong to the same irreducible representation.

For analyzing the effect of occupied-virtual orbital mixing based on the electron density, the first-order one-electron density variation is expressed using CMOs as:[26]

$$\rho_{\mathrm{VO}}^{(1)} = \sum_{i,a} \mathrm{U}_{ai}^{(1)*} \psi_a^* \psi_i + \mathrm{U}_{ai}^{(1)} \psi_i^* \psi_a \quad (21)$$

Using the NROs, this equation is represented as

$$\rho_{\mathrm{VO}}^{(1)} = \sum_{i} n_i \lambda_i (\phi_i'^* \phi_i + \phi_i' \phi_i^*). \quad (22)$$

This equation simplifies the feature of the one-electron density variation. For the real part of the product of the NRO pair, the one-electron density increases in the in-phase region and decreases in the anti-phase region. **Figure 7** draws the product of the occupied and virtual NROs with the highest contribution at the ET-TS structure in the forward and reverse directions of the IRC. The yellow and cyan parts indicate the regions of increasing and decreasing one-electron density, respectively. Note that the sign of the one-electron density variation is opposite for the forward or reverse directions, because as explained in Sec. II, the phase of each NRO pair becomes opposite for the reverse nuclear displacement direction. Figure 7 also indicates that the electron transfer proceeds from π^*_{CO} of the formaldehyde anion to $\sigma^*_{\mathrm{C\text{-}Cl}}$ of methyl chloride in the forward reaction and that the opposite electron transfer progresses in the reverse reaction, as expected from Fig. 6. As described in Sec. II, reversing the phase of one orbital in the NRO pair turns over the phase of another orbital, in definition. Therefore, because the phase reversal of the NRO pair is carried out as $(\phi_i, \phi_i') \rightarrow (-\phi_i, -\phi_i')$, the sign of $\rho_{\mathrm{VO}}^{(1)}$ in Eq. (22) is always kept invariant. More generally, $\rho_{\mathrm{VO}}^{(1)}$ is invariant for the phase rotation of the NRO pair such as $(\phi_i, \phi_i') \rightarrow (\phi_i e^{i\theta}, \phi_i' e^{i\theta})$, where θ denotes arbitrary phase angle, and therefore, $\rho_{\mathrm{VO}}^{(1)}$ is uniquely determined for any nuclear displacement. The discussion in Fig. 6 is also not affected by the phase reversal of the NROs. This consistency comes from the nature of the U matrix, which

is a solution to the CPSCF equation. Note that, unlike CMO, NRO implicitly includes the information of nuclear displacement *via* the U matrix of the CPSCF equation. The simple relationship with the one-electron density change during nuclear displacement is one of the most important features of NRO.

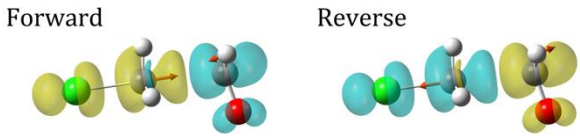

Figure 7. Images of the product of NRO pairs (ϕ_1^{α} and $\phi_1'^{\alpha}$) with maximum singular values associated with forward and reverse nuclear displacements along the imaginary frequency mode indicated by red vector arrows at the ET-TS of the H_2CO^- + CH_3Cl reaction. The increase and decrease in one-electron density are indicated by yellow and cyan regions, respectively.

So far, we have discussed NRO at ET-TS based on the assumption that electron transfer occurs at the transition state. **Figure 8** shows the variation of the sum of squared singular values of the $\mathbf{U}_{\mathrm{VO}}^{(1)}$ matrices of α- and β-spin orbitals ($\| \mathbf{\Lambda}^{\alpha} \|_F^2 = \sum_i \lambda_i^{\alpha 2}$ and $\| \mathbf{\Lambda}^{\beta} \|_F^2 = \sum_i \lambda_i^{\beta 2}$) with the change in nuclear coordinates along the reaction coordinate *s* throughout the IRC. The figure clearly illustrates that there are two places where $\| \mathbf{\Lambda}^{\alpha} \|_F^2$ and $\| \mathbf{\Lambda}^{\beta} \|_F^2$ show sharp peaks along the IRC: the first peak is found near the transition state structure ($\| \mathbf{\Lambda}^{\alpha} \|_F^2$ = 0.813 and $\| \mathbf{\Lambda}^{\beta} \|_F^2$ = 0.091 at *s* = 0.47 amu$^{1/2}$ bohr), and the second peak is found near the shoulder shape of the potential energy ($\| \mathbf{\Lambda}^{\alpha} \|_F^2 =$ 0.032 and $\| \mathbf{\Lambda}^{\beta} \|_F^2$ = 0.109 at *s* = 4.49 amu$^{1/2}$ bohr). The former peak indicates that α-spin electron is mainly transferred near the TS structure, while the latter peak indicates that β-spin electron is mainly transferred successively. It is confirmed that the dominant NRO pair at *s* = 0.47 amu$^{1/2}$ bohr is almost the same as that at the ET-TS structure. It is very interesting to note that for a given elementary reaction, the features in the potential energy profile such as transition states and shoulders reflect the large response of the electron distribution to the nuclear displacement of the molecule. This result suggests that the singular value of the $\mathbf{U}_{\mathrm{VO}}^{(1)}$ matrix explains the physical meaning of the TS structure from the viewpoint of the electronic theory.

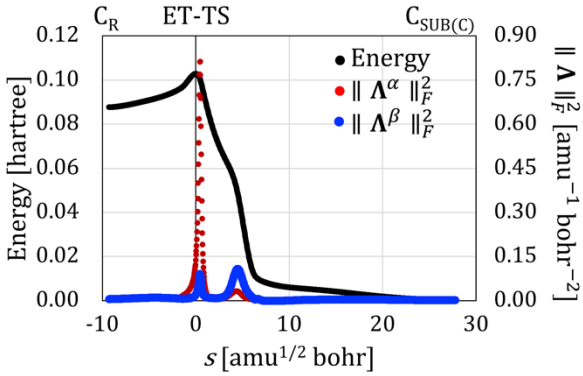

Figure 8. Potential energy along the IRC of the H_2CO^- + CH_3Cl reaction, for which the energy of the product, $C_{SUB(C)}$, is set to be zero, and the $\| \mathbf{\Lambda}^{\alpha} \|_F^2$ and $\| \mathbf{\Lambda}^{\beta} \|_F^2$ values. The first peak of $\| \mathbf{\Lambda}^{\alpha} \|_F^2$ near the ET-TS structure (0.47 amu$^{1/2}$ bohr) mainly corresponds to the α-NRO pair of Fig. 3 and the second peak of $\| \mathbf{\Lambda}^{\beta} \|_F^2$ at the shoulder of the potential energy (4.49 amu$^{1/2}$ bohr) corresponds to the β-NRO pair.

Figure 9 shows the NROs with large contributions in the region where $\| \mathbf{\Lambda}^{\alpha} \|_F^2$ and $\| \mathbf{\Lambda}^{\beta} \|_F^2$ show a peak, *i.e.*, at the ET-TS structure and the shoulder of the potential, with the valence bond configuration mixing (VBCM) diagram of this reaction by Shaik *et al.*[33–36]. The VBCM diagram, which was constructed based on the valence bond theory instead of the MO theory, suggested that the π*-SOMO of formaldehyde anion (π^*_{CO}) and the σ*-LUMO of methyl chloride ($\sigma^*_{C\text{-}Cl}$) play a major role in the electron transfer at ET-TS structure.[33] Note that the contribution of π^*_{CO} and $\sigma^*_{C\text{-}Cl}$ is not easily derived from the CMOs due to the highly-delocalized nature of the virtual CMOs, as seen in Fig. 2. On the other hand, the current NRO analysis extracts NRO pairs that are easily mixing under nuclear displacements along the reaction path. Therefore, this analysis can verify the VBCM result based on the MO theory. The NRO analyses using the dominant NRO products reveal the reaction processes at the ET-TS structure and the potential shoulder as the C-Cl bond dissociation by the electron transfer from H_2CO^- to H_3CCl (see $\phi_1^{\alpha}\phi_1'^{\alpha}$) and the formation of the C-C σ bond by the CH_3 radical attacking H_2CO (see $\phi_1^{\alpha}\phi_1'^{\alpha}$ and $\phi_1^{\beta}\phi_1'^{\beta}$), respectively. These results are in good agreement with the VBCM analysis on the basis of electron transfers between π^*_{CO} and $\sigma^*_{C\text{-}Cl}$ (or n_C).[35] Note that conventional reaction analyses based only on the energy profile may incorrectly interpret this reaction as the concerted S_N2 reaction. Instead, this NRO analysis reveals that this H_2CO^- + CH_3Cl reaction consists of two asynchronous electron transfers.

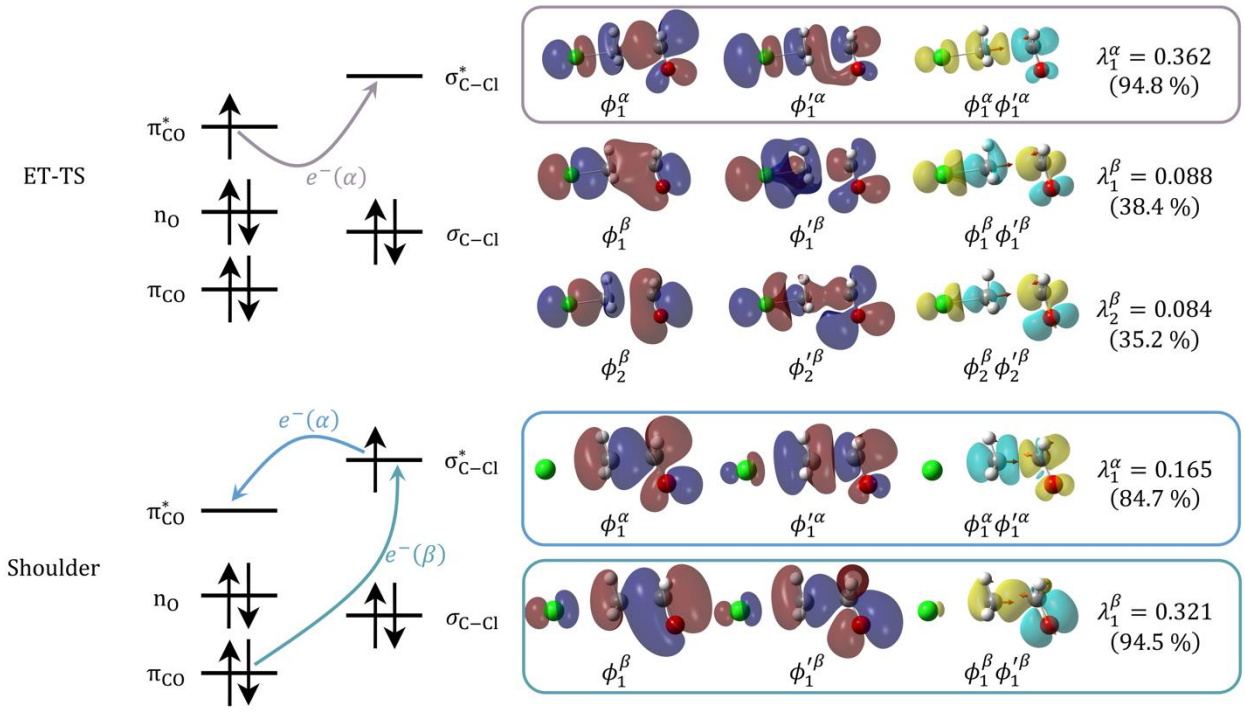

Figure 9. Dominant NROs at the two sharp peaks of $\| \mathbf{\Lambda}^\alpha \|_F^2$ and $\| \mathbf{\Lambda}^\beta \|_F^2$, the ET-TS structure and the shoulder of the potential at 4.49 amu$^{1/2}$ bohr on the IRC in Fig. 8, with the valence bond configuration mixing diagram of this reaction in Ref. 35. Images of products of the NRO pairs are also illustrated with the vector arrows corresponding to the nuclear displacements. For the products, the yellow and cyan regions show the increase and decrease of the one-electron density, respectively. The singular values and contribution ratios for the dominant NRO pairs are shown at the rightmost.

One of the greatest advantages of the NRO analysis is to automatically extract the orbitals that play an important role in chemical reactions, even without knowledge of organic chemistry. Actually, the NRO pairs are generated without selecting valence bond orbitals as different from the VBCM method. Therefore, the NRO analysis can upgrade electronic theory-based reaction analyses.

B. Claisen rearrangement

Next, the NRO analysis is applied to the Claisen rearrangement reaction of $C_3H_5OC_2H_3$ molecule. **Figure 10** shows the energy profile (in black) and the sum of squared singular values of $\mathbf{U}_{\mathrm{VO}}^{(1)}$, $\| \mathbf{\Lambda} \|_F^2 = \sum_i \lambda_i^2$, (in red) along the IRC at the B3LYP/6-311+G(d,p) level. As shown in the figure, $\| \mathbf{\Lambda} \|_F^2$ has a peak near the TS structure. Though large $\| \mathbf{\Lambda} \|_F^2$ are also given for the reactant and product regions, they come from relatively insignificant conformational changes. **Figure 11** shows the dominant NRO pairs at the TS structure: ϕ_1 and ϕ_1' with λ_1 = 0.228 amu$^{-1/2}$ bohr^{-1} (contribution ratio = 52.0%) and ϕ_2 and ϕ_2' with λ_2 = 0.187 amu$^{-1/2}$ bohr^{-1} (contribution ratio = 35.1%). These two sets of NROs cover 87.1 % of the virtual-occupied mixing. The NRO product, $\phi_1\phi_1'$, shows the increase and decrease of density in C-C π bond regions of the C_3H_5 and OC_2H_3 fragments, respectively. On the other hand, $\phi_2\phi_2'$ shows the increase of density in the region of C-C σ bond to be formed and the decrease in the region of C-O σ bond to be cleaved. The figure also shows a slight density increase in C-O π bond region. Note that these density changes correctly characterize the bond rearrangements. It is, therefore, confirmed that NRO analysis succeeds in revealing reactive orbitals in the Claisen rearrangement reaction of $C_3H_5OC_2H_3$ molecule.

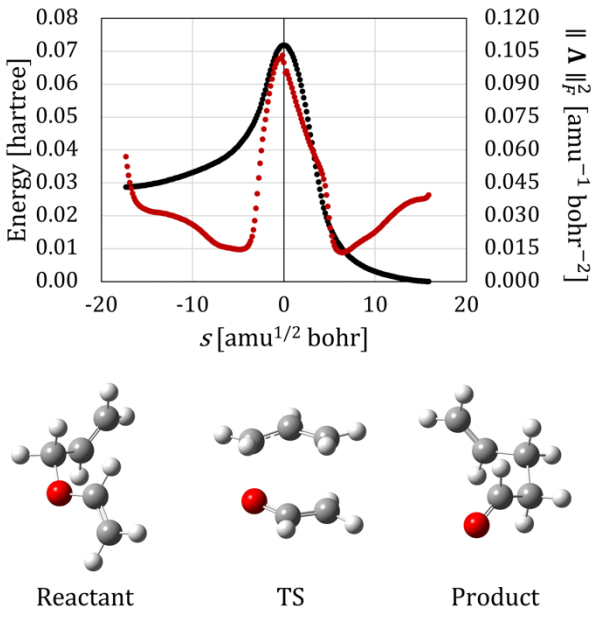

Figure 10. Potential energy profile (black dots) and $\| \mathbf{\Lambda} \|_F^2$ (red dots) for the IRC of the Claisen rearrangement reaction of $C_3H_5OC_2H_3$ molecule, for which the product energy is set to be zero. The molecular structures of the reactant, TS, and product are also shown below.

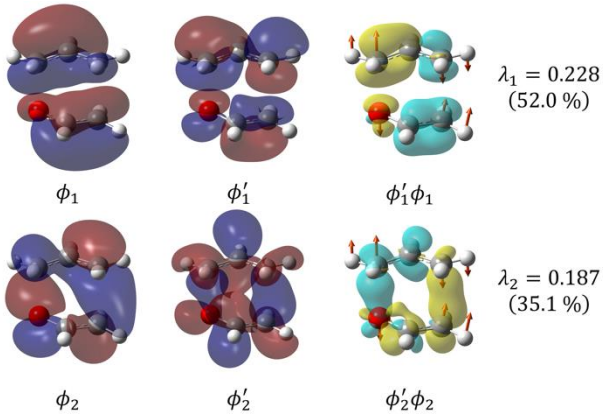

Figure 11. NRO pairs with the maximum and second maximum singular values and their products at the TS structure of the Claisen rearrangement reaction. The products of the NRO pairs are shown with the transition vectors of imaginary frequency.

C. Diels-Alder reaction

The NRO analysis is also examined for the Diels-Alder reaction of 1,3-butadiene and nitroethylene. **Figure 12** shows the energy profile (in black) and the sum of squared values of $\mathbf{U}_{\mathrm{VO}}^{(1)}$, $\| \mathbf{\Lambda} \|_F^2$, (in red) along the IRC calculated at the RHF/6-31G(d,p) level. As shown in the figure, $\| \mathbf{\Lambda} \|_F^2$ has peaks at X (s = −10.90 amu$^{1/2}$ bohr) and near the TS (s = 0). What we should notice is that the point X, a local maximum of $\| \mathbf{\Lambda} \|_F^2$, does not correspond to a shoulder of the total energy profile. **Figure 13a** shows the dominant NRO pairs at X: ϕ_1 and ϕ_1' with λ_1 = 0.152 amu$^{-1/2}$ bohr^{-1} (contribution ratio = 53.8%) and ϕ_2 and ϕ_2' with λ_2 = 0.091 amu$^{-1/2}$ bohr^{-1} (contribution ratio = 19.5%). These two sets of NROs cover 73.3 % of the virtual-occupied mixing in total. At the point X, the mixing of NROs comes from the twist motion of butadiene causing density variation, which is not essential in the Diels-Alder reaction. **Figure 13b** shows the dominant NRO pairs at the TS structure: ϕ_1 and ϕ_1' with λ_1 = 0.390 amu$^{-1/2}$ bohr^{-1} (contribution ratio = 51.3%) and ϕ_2 and ϕ_2' with λ_2 = 0.357 amu$^{-1/2}$ bohr^{-1} (contribution ratio = 43.0%). These two sets of NROs cover 94.3 % of the virtual-occupied mixing in total. As shown in the figure, the two NRO products clearly show that the density increases in the region of two C-C σ bonds to be formed. The figure also indicates that the density slightly increases in the region of the C2-C3 π bond of butadiene, indicating the formation of the C2-C3 π bond. On the other hand, the electron density decreases in the regions of C1-C2 π bond and C3-C4 π bond, causing the C-C π bond cleavage. The density changes, therefore, correctly represent the bond rearrangements of the Diels-Alder reaction. Interestingly, the density changes in the Diels-Alder reaction between 1,3-butadiene and nitroethylene are different from those of the reaction between 1,3-butadiene and ethylene, as shown in **Fig. 14**. This difference

shows that the substituent nitro group significantly affects the electron mobilities even in similar types of reactions. This indicates that the NRO analysis can clearly reveal the electronic effect of substituents in reactions.

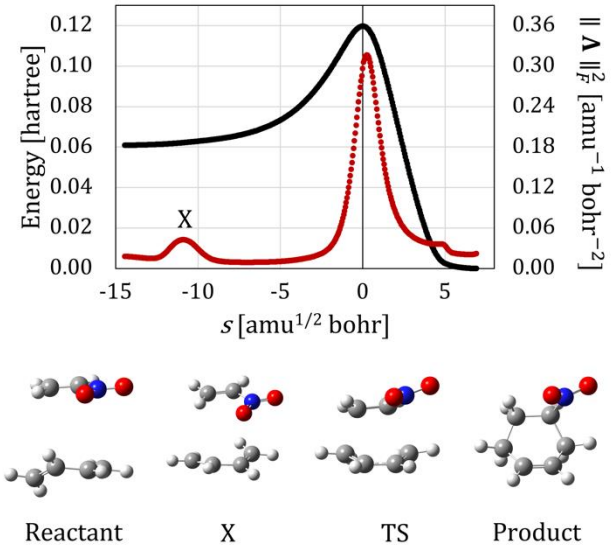

Figure 12. Potential energy profile (black dots) and $\| \mathbf{\Lambda} \|_F^2$ (red dots) for the IRC of the Diels-Alder reaction of 1,3-butadiene and nitroethylene. The structures at the reactant, point X, TS, and product are also shown below.

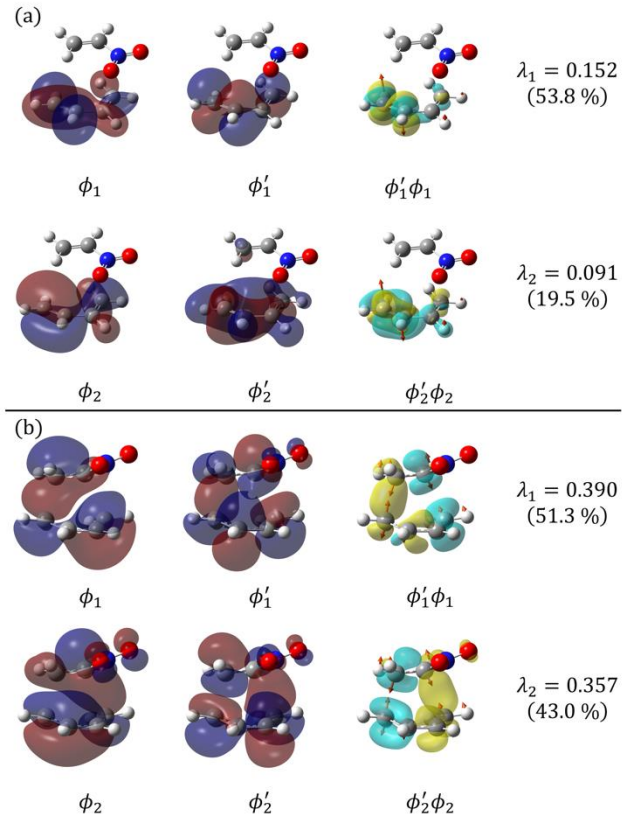

Figure 13. NRO pairs of the maximum and second maximum singular values and their products, which are calculated (a) at the point X and (b) at the TS structure on the IRC of the Diels-Alder reaction of 1,3-butadiene and nitroethylene. The products of the NRO pairs are also shown with the tangent vector of the IRC. For the NRO products, the yellow and cyan regions indicate the increase and decrease of the one-electron density, respectively.

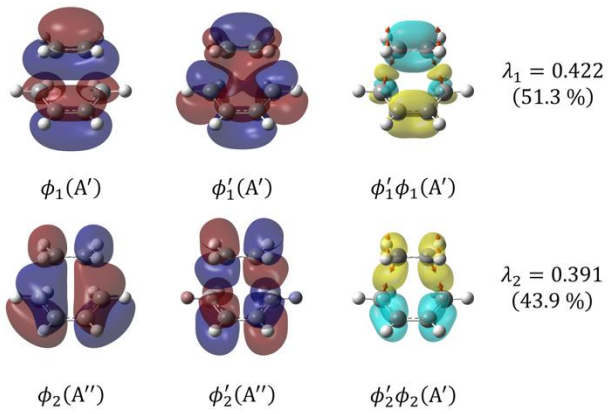

Figure 14. NRO pairs of the maximum singular value (ϕ_1 and ϕ_1') and the second maximum singular value (ϕ_2 and ϕ_2'), which are calculated at the TS structure (C_s point group) with the imaginary frequency mode of A' symmetry, in the Diels-Alder reaction of ethylene and 1,3-butadiene at the RHF/6-31G(d,p) level. The products of the NRO pairs are also shown with the tangent vector of the IRC. For the NRO products, the yellow and cyan regions indicate the increase and decrease of the one-electron density, respectively. The singular value of the (ϕ_1, ϕ_1') pair is 0.422 amu$^{-1/2}$ bohr^{-1} (contribution: 51.3%), while that of the (ϕ_2, ϕ_2') pair is 0.391 amu$^{-1/2}$ bohr^{-1} (contribution: 43.9%). Note that these two sets of NROs cover 95.2 % of the description of orbital mixing at the TS structure.

D. Proton transfer in malonaldehyde

Next, the NRO analysis is carried out for the intramolecular proton transfer in malonaldehyde. **Figure 15** shows the energy profile and the sum of squared singular values of $\mathbf{U}_{\mathrm{VO}}^{(1)}$, $\| \mathbf{\Lambda} \|_F^2$, along the IRC calculated at LC-BLYP/6-311+G(d,p) level.[7] As shown in the figure, $\| \mathbf{\Lambda} \|_F^2$ has only one peak near the TS structure (0.00 amu$^{1/2}$ bohr). **Figure 16** shows the dominant NRO pairs at the TS structure: ϕ_1 and ϕ_1' with λ_1 = 0.572 amu$^{-1/2}$ bohr^{-1} (contribution ratio = 49.9%) and ϕ_2 and ϕ_2' with λ_2 = 0.523 amu$^{-1/2}$ bohr^{-1} (contribution ratio = 41.7%). These two sets of NROs cover 91.6 % of the virtual-occupied mixing in total. The NRO product $\phi_1\phi_1'$ shows that the density decreases and increases in the left and right C-C π bond regions, respectively. This corresponds to the C-C π bond shift from the left to the right bonds. On the other hand, the NRO product $\phi_2\phi_2'$ shows that the density increases and decreases on the left and right oxygens, respectively. The density increases in the p-type orbital of the left oxygen atom are interpreted as the electron transfer to the left oxygen shared with

the hydrogen atom to cleave the O-H bond. On the other hand, the density decreases in the p-type orbital of the right oxygen atom to share its lone pair with the hydrogen atom in the formation of the O-H bond.

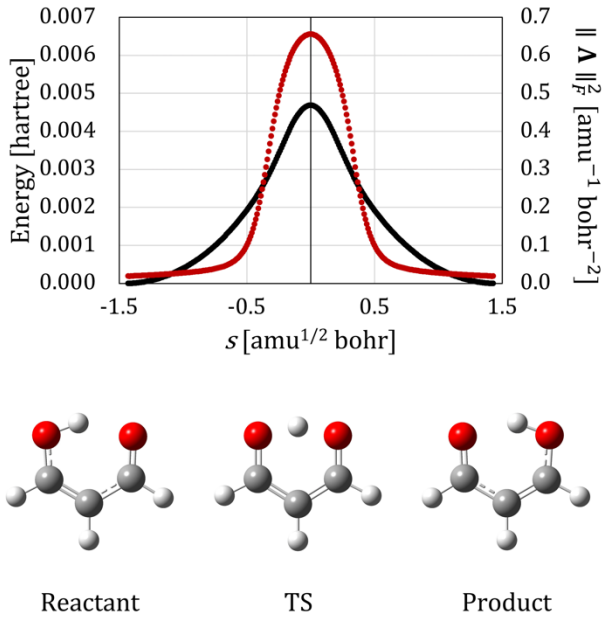

Figure 15. Potential energy profile (black dots) and $\| \mathbf{\Lambda} \|_F^2$ (red dots) for the IRC of the intramolecular proton transfer in malonaldehyde. The structures at the reactant (C_s), TS (C_{2v}), and product (C_s) are also shown below.

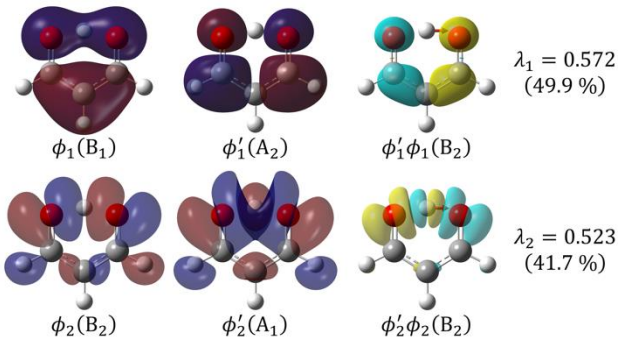

Figure 16. NRO pairs of the maximum singular value (ϕ_1 and ϕ_1') and the second maximum singular value (ϕ_2 and ϕ_2'), which are calculated at the TS structure (C_{2v}) in Fig. 15 for the proton transfer in malonaldehyde. The products of the NRO pairs are shown with the transition vectors of an imaginary frequency (B_2 symmetry). Irreducible representations of NROs and NRO products are also shown.

It is interesting to comparatively discussing the NRO method with the bonding evolution theory (BET),[50] which interprets elementary chemical processes based on topological changes of the electron localization function (ELF)[51] along a

reaction path. For the proton transfer reaction of malonaldehyde, the BET analysis shows that the covalent O-H bond is cleaved at 1.105 Å at the bifurcation point of the ELF, while a new ELF minimum appears between oxygen and hydrogen on the left side, which corresponds to the cleavage of the O-H bond, at this bifurcation point.[52] Note that this ELF topological change is interpreted to reflect a decrease in the electron density between the left-side oxygen and hydrogen, as similar to the discussion based on the product of the NRO pair, $\phi_2\phi_2'$, in Fig. 16. That is, the NRO analysis provides similar interpretations to the topological changes of the ELF for the proton transfer reaction of malonaldehyde. What we would emphasize is that the NRO method automatically extracts the reacting orbital pairs showing similar pictures of this reaction. This is a major advantage of the NRO method.

E. 1,2-alkyl shift/nitrene addition

The NRO analysis is also examined for the 1,2-alkyl shift/nitrene addition.[53] **Figure 17** shows the energy profile and the sum of squared singular values of $\mathbf{U}_{\mathrm{VO}}^{(1)}$, $\| \mathbf{\Lambda} \|_F^2$, along the IRC calculated at the B3LYP/6-311++G(d,p) level. As shown in the figure, $\| \mathbf{\Lambda} \|_F^2$ has peaks at the shoulder of the profile ($s = -7.95$ amu$^{1/2}$ bohr) and near the TS structure ($s = 0$). Note that this reaction consists of two asynchronous processes, though it gives no intermediate. **Figure 18a** shows the dominant NRO pairs at the shoulder: ϕ_1 and ϕ_1' with λ_1 = 0.571 amu$^{-1/2}$ bohr^{-1} (contribution ratio = 94.0%) and ϕ_2 and ϕ_2' with λ_2 = 0.114 amu$^{-1/2}$ bohr^{-1} (contribution ratio = 3.8%). These two sets of NROs cover 97.8% of the virtual-occupied mixing in total. Since the pair of ϕ_1 and ϕ_1' has a predominantly large contribution, the electron transfer at the TS structure is supposed to proceed almost only between this pair. This figure shows that the 1,2-alkyl shift (C-N bond cleavage and C-C bond formation) proceeds at the potential shoulder. The NRO products, $\phi_1\phi_1'$ and $\phi_2\phi_2'$, show the density decrease in the C-N σ bond region and increase in the C-C σ bond region, respectively. Therefore, the mixture of ϕ_1 and ϕ_1' contributes to the C-N bond cleavage while the mixture of ϕ_2 and ϕ_2' contributes to the C-C bond formation. It is, however, considered that the C-N bond cleavage mainly proceeds at the shoulder, because the contribution ratio of ϕ_1 and ϕ_1' is much larger than that of ϕ_2 and ϕ_2'. On the other hand, the C-C bond formation is supposed to proceed at the TS structure as shown for $\phi_1\phi_1'$ in **Fig. 18b**. Figure 18b shows the dominant NRO pairs at the TS structure: ϕ_1 and ϕ_1' with λ_1 = 0.241 amu$^{-1/2}$ bohr^{-1} (contribution ratio = 57.6%) and ϕ_2 and ϕ_2' with λ_2 = 0.160 amu$^{-1/2}$ bohr^{-1} (contribution ratio = 25.6%). These two sets

of NROs cover 83.2% of the virtual-occupied mixing in total. Note that the nitrene addition proceeds around the TS structure. The NRO product $\phi_1\phi_1'$ shows that the density increases corresponding to the C-C bond formation through the 1,2-alkyl shift initiated around the shoulder. The product $\phi_1\phi_1'$ also shows that the density increases between the nitrogen and one of the α-carbon, while it decreases between the carbonyl carbon and the α-carbon. Therefore, electrons between the carbonyl carbon and the α-carbon are withdrawn by the nitrogen to form a σ bond between nitrogen and the α-carbon. On the other hand, the product $\phi_2\phi_2'$ shows that the density decreases on the nitrogen, while it increases between the nitrogen and the carbonyl carbon. Electrons on the nitrogen are, therefore, withdrawn by the carbonyl group to form a σ bond between nitrogen and the carbonyl carbon.

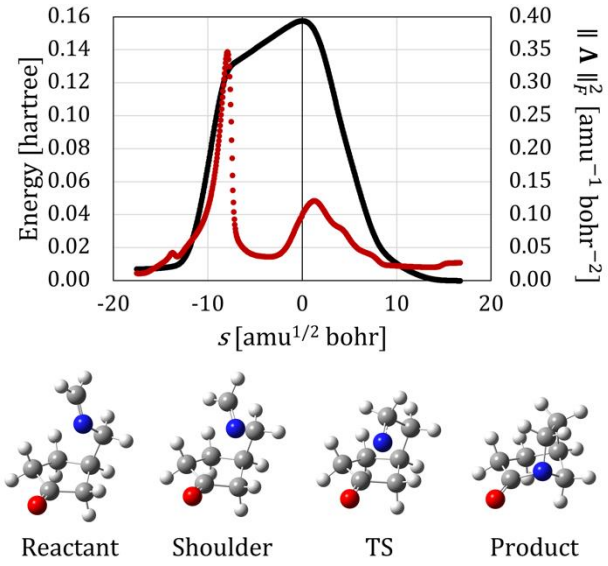

Figure 17. Potential energy profile (black dots) and $\| \mathbf{\Lambda} \|_F^2$ (red dots) for the IRC of 1,2-alkyl shift/nitrene addition. The structures at the reactant, shoulder, TS, and product are also shown below.

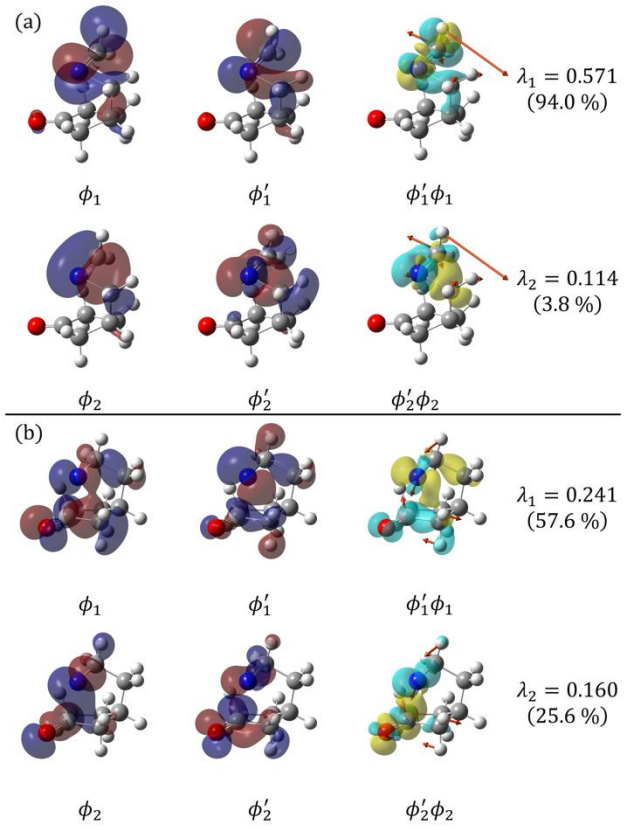

Figure 18. NRO pairs of the maximum singular value (ϕ_1 and ϕ_1') and the second maximum singular value (ϕ_2 and ϕ_2'), which are calculated (a) at the shoulder and (b) at the TS in Fig. 17 of 1,2-alkyl shift/nitrene addition. The products of the NRO pairs are shown with the tangent vectors of the IRC.

F. Carbocation rearrangement

Finally, the NRO analysis is applied to the carbocation rearrangement reaction of cyclohexyl cation to methylcyclopentyl cation, which includes multiple bond rearrangement.[54,55] **Figure 19** illustrates the energy profile and the sum of squared singular values of $\mathbf{U}_{\mathrm{VO}}^{(1)}$, $\| \mathbf{\Lambda} \|_F^2$, which are calculated at the B3LYP/6-311G(d,p) level with a net charge +1. As shown in the figure, the $\| \mathbf{\Lambda} \|_F^2$ value has a peak near the TS structure (s = 0) and at the point X (s = 2.00 amu$^{1/2}$ bohr), though the energy profile shows no shoulder behavior at the point X. This shoulder-less behavior is attributed to the nature of this reaction, in which two asynchronous processes take place without intermediates. **Figure 20a** shows the dominant NRO pairs at the TS structure: ϕ_1 and ϕ_1' with λ_1 = 0.436 amu$^{-1/2}$ bohr^{-1} (contribution ratio = 90.0%) and ϕ_2 and ϕ_2' with λ_2 = 0.106 amu$^{-1/2}$ bohr^{-1} (contribution ratio = 5.4%). These two NRO sets cover 95.4% of the virtual-occupied mixing in total. Since the pair of ϕ_1 and ϕ_1' has a predominantly large contribution, the electron transfer at the TS structure is supposed to proceed almost

only between this pair. As shown in the figure, the NRO product $\phi_1\phi_1'$ shows the density decrease on the hydride donating carbon (denoted as b), while it shows electron density increase between the carbon atoms (denoted as b and c) to form a C-C σ bond. As a result, the mixture of ϕ_1 and ϕ_1' contributes to both the C-H bond cleavage and C-C σ bond formation. **Figure 20b** shows the dominant NRO pairs at X, ϕ_1 and ϕ_1' with λ_1 = 0.336 amu$^{-1/2}$ bohr^{-1} (contribution ratio = 78.1%) and ϕ_2 and ϕ_2' with λ_2 = 0.143 amu$^{-1/2}$ bohr^{-1} (contribution ratio = 14.2%). These two sets of NROs cover 92.3% of the virtual-occupied mixing in total. The NRO product $\phi_1\phi_1'$ shows that the density decreases on the hydride donating carbon (denoted as b), while it increases on the hydride accepting carbon (denoted as a), respectively. On the other hand, $\phi_2\phi_2'$, shows that the density increases on the hydride donating carbon (denoted as b), while it decreases on the hydride accepting carbon (denoted as a), respectively. As a consequence, the mixture of ϕ_1 and ϕ_1' contributes to the 1,2-hydride shift, while the mixture of ϕ_2 and ϕ_2' may stabilize the carbocation center by hyperconjugation.

Figure 19 shows that the potential energy has no shoulder at the point X, where $\| \mathbf{\Lambda} \|_F^2$ has a peak, even though this reaction contains dual bond rearrangement. This indicates that the NROs are much more sensitive than the potential energy surface for describing the reaction mechanism. As mentioned above, the NROs of the maximum singular values in Fig. 20 correctly represent the C-H bond cleavage, C-C bond formation, and 1,2-hydride shift, which are required to proceed with this rearrangement reaction, though the 1,2-hydride shift is not detected in the potential energy profile. For all the calculated reactions, we have shown that the NRO analyses reasonably explain the reaction mechanisms from the viewpoint of the electronic theory. We, therefore, conclude that the NRO analysis can reveal more sophisticated chemical reaction mechanisms than those of the energy profiles.

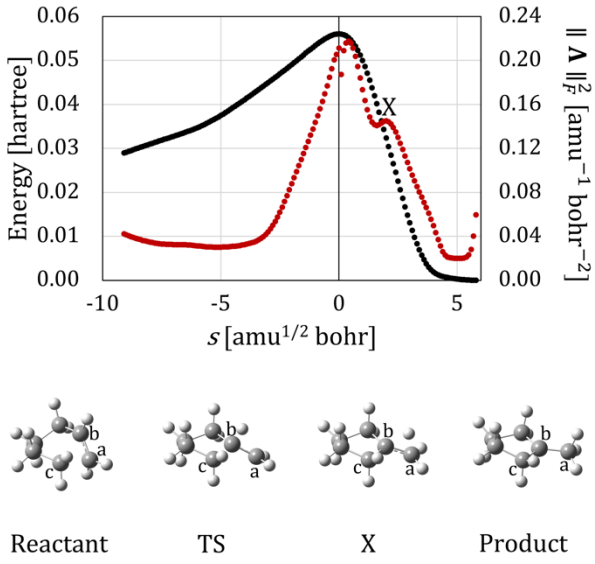

Figure 19. Potential energy profile (black dots) and $\| \mathbf{\Lambda} \|_F^2$ (red dots) for the IRC of the carbocation rearrangement reaction of cyclohexyl cation to methylcyclopentyl cation. The structures at the reactant, TS, X, and product are also shown below.

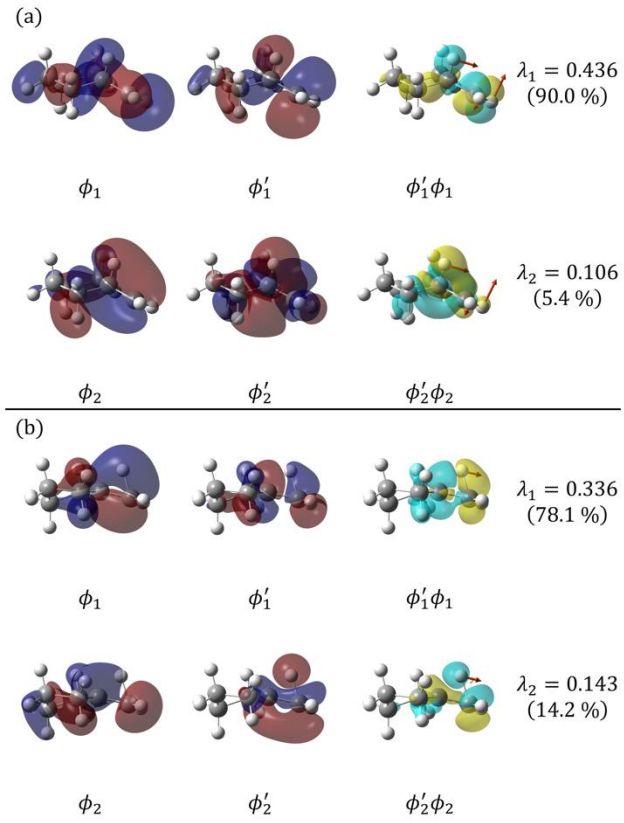

Figure 20. NRO pairs of the maximum singular value (ϕ_1 and ϕ_1') and the second maximum singular value (ϕ_2 and ϕ_2'), which are calculated (a) at the TS structure and (b) at the point X in Fig. 19 for carbocation rearrangement. The products of the NRO pairs are shown with the tangent vectors of the IRC.

IV. Conclusions

In this study, we propose natural reaction orbital (NRO) as a sophisticated tool for analyzing chemical reactions from the viewpoint of the electronic theory. The NRO-based reaction analysis method has five distinctive advantages for availability and applicability:

1. The NRO pairs that drive the chemical reaction are automatically extracted based on the nuclear coordinate derivative of the canonical MOs obtained by solving the CPSCF equation. Since the extraction process is fully automated, no empirical intuition or in-depth knowledge other than the calculated results is required to determine the reactive orbitals.
2. The delocalization of virtual canonical orbitals, which complicates orbital-based reaction analysis, is dramatically improved in virtual NRO.
3. Since NRO can be calculated for any given molecular structure, it reduces the effort to analyze the important electron transfer in chemical reaction paths.
4. NRO is highly robust due to its low dependence on the basis set (Fig. 5).
5. If the nuclear displacement from a given molecular structure belongs to an irreducible representation of a point group, then the NRO also belongs to one of irreducible representations of the point group, and the NRO pair can have a nonzero singular value only if the direct product of the irreducible representations of the nuclear displacement, the occupied NRO, and the virtual NRO is totally symmetric.

Note that the NRO-based reaction analysis is the only method that satisfies all of these advantages among similar orbital-based analysis methods.

Applying the NRO-based analysis method to the H_2CO^- + H_3CCl reaction, it was found that the sum of the squared singular values, $\| \mathbf{\Lambda} \|_F^2$, provides a local maximum sharp peak around the transition state structure, indicating the C-Cl bond dissociation by the electron transfer from H_2CO^- to H_3CCl. It was also found that another sharp peak is provided at the shoulder of the potential energy profile, which corresponds to the formation of the C-C σ bond by the CH_3 radical attacking H_2CO. This electronically reveals the asynchronous processes of this reaction. Following this result, the NRO-based analysis method was also applied to five reactions including multiple bond rearrangement. It was found that $\| \mathbf{\Lambda} \|_F^2$ gives a peak near the transition state structures for all the calculated reactions. This indicates the physical meaning of transition state from the viewpoint of the electronic theory. It is also found that $\| \mathbf{\Lambda} \|_F^2$ also provides peaks at the places where the potential energy

profiles have shoulder features for many reactions, though there are a few reactions, for which $\| \mathbf{\Lambda} \|_F^2$ gives a peak at the place where the potential energy profile has no shoulder. We, therefore, concluded that the NROs are much more sensitive than the potential energy surface for representing reaction mechanisms.

In summary, it is confirmed that the NRO-based reaction analysis method has universality and robustness, and therefore, the NRO analysis becomes a powerful tool for describing sophisticated reaction mechanisms. Automation of reactive orbitals extraction, conventionally conducted manually by chemists, is expected to contribute to optimize the researching process and to accelerate multidisciplinary collaborations with other fields. We hope that this NRO analysis will lead to universal reaction analyses based on the electronic theory.

Appendix

In this section, we compile the procedure for performing the NRO analysis using the results of Gaussian 16 program. As an example, let us consider the NRO analysis at the TS structure of a system consisting of N atoms based on the Hartree-Fock calculation:

1. First, optimize the TS geometry.
2. Perform the frequency calculation at the optimized TS geometry with several options: e.g., Freq=HPModes and IOp(5/33=2, 10/21=1, 10/33=2).
3. Extract the necessary data from the Gaussian logfile: i.e., the normal mode vector with imaginary frequency, the MO coefficients, and the **U** matrices of the CPHF calculations (which are given below "CPHF results for **U** (alpha)" or "CPHF results for **U** (beta)"). There are $3(N+1)$ **U** matrices depending on the degrees of freedom of the electric field and N atoms. Note that the first three matrices are unnecessary, because they correspond to the perturbations of the electric field.
4. Calculate the inner product of the normal mode vector with imaginary frequency with the $3N$ **U** matrices for the degrees of freedom of the N nuclei. Note that the normal mode vectors should be orthonormalized in mass-weighted coordinates and the units of the **U** matrix should be converted to the mass-weighted atomic unit. It should also be confirmed that both are given in the same orientation ("Standard orientation" or "Input orientation").
5. Perform singular value decomposition (SVD) for the matrix generated in step 4, using a library such as DGESVD of

LAPACK.[56]

6. Finally, carry out the unitary transformation of the MO coefficients by the left-singular and right-singular vectors (see Eqs. (17)-(19) in Sec. II). Note that the occupied and virtual MO coefficients are separately transformed. The transformed coefficients become the NRO coefficients.

The NROs can be visualized by replacing the MO coefficients in the fchk file with the generated NRO coefficients using an MO visualizer like GaussView.[57] Note that if the NROs are evaluated at a non-TS point, the normal mode vector with imaginary frequency must be replaced by the IRC tangent vector, i.e., the gradient vector of the potential energy surface, which is normalized in the mass-weighted coordinates.

Conflicts of interest

There are no conflicts to declare.

Acknowledgements

SE thanks the Institute for Quantum Chemical Exploration through the Research Fellowship for Young Scientists and the MEXT Doctoral program for DataRelated InnoVation Expert Hokkaido University (D-DRIVE-HU). This work was also partly supported by the Elements Strategy Initiative of MEXT (JPMXP0112101003), the Photoexcitonix Project at Hokkaido University, and JST CREST, Japan (JPMJCR1902). A part of calculations was performed using the Research Center for Computational Science, Okazaki, Japan.

Notes and references

[1] K. Ohno, H. Mutoh, and Y. Harada, *J. Am. Chem. Soc.*, 1983, **105**, 4555.

[2] M. Yamazaki, T. Horio, N. Kishimoto, and K. Ohno, *Phys. Rev. A*, 2007, **75**, 032721.

[3] E. Weigold and I. E. McCarthy, *Electron Momentum Spectroscopy*, Springer, US, Boston, MA, 1999.

[4] J. Itatani, J. Levesque, D. Zeidler, H. Niikura, H. Pépin, J.C. Kieffer, P.B. Corkum, and D.M. Villeneuve, *Nature*, 2004, **432**, 867.

[5] P. Puschnig, E.-M. Reinisch, T. Ules, G. Koller, S. Soubatch, M. Ostler, L. Romaner, F.S. Tautz, C. Ambrosch-Draxl, and M.G. Ramsey, *Phys. Rev. B*, 2011, **84**, 235427.

[6] J.P. Perdew, R.G. Parr, M. Levy, and J.L. Balduz, *Phys. Rev. Lett.*, 1982, **49**, 1691.

[7] H. Iikura, T. Tsuneda, T. Yanai, and K. Hirao, *J. Chem. Phys.*, 2001, **115**, 3540.

[8] L.J. Sham and M. Schlüter, *Phys. Rev. B*, 1985, **32**, 3883.

[9] T. Tsuneda, J.W. Song, S. Suzuki, and K. Hirao, *J. Chem. Phys.*, 2010, **133**, 174101.

[10] K. Fukui, T. Yonezawa, and H. Shingu, *J. Chem. Phys.*, 1952, **20**, 722.

[11] K. Fukui, T. Yonezawa, and C. Nagata, *Bull. Chem. Soc. Jpn.*, 1954, **27**, 423.

[12] R.B. Woodward and R. Hoffmann, *J. Am. Chem. Soc.*, 1965, **87**, 395.

[13] R. Hoffmann and R.B. Woodward, *J. Am. Chem. Soc.*, 1965, **87**, 2046.

[14] R. Hoffmann and R.B. Woodward, *J. Am. Chem. Soc.*, 1965, **87**, 4388.

[15] R.B. Woodward and R. Hoffmann, *Angew. Chemie Int. Ed. English*, 1969, **8**, 781.

[16] R. Hoffmann and R.B. Woodward, *Science*, 1970, **167**, 825.

[17] P. Geerlings, F. De Proft, and W. Langenaeker, *Chem. Rev.*, 2003, **103**, 1793.

[18] T. Tsuneda and R.K. Singh, *J. Comput. Chem*., 2014, **35**, 1093.

[19] T. Tsuneda, R.K. Singh, and P.K. Chattaraj, *Phys. Chem. Chem. Phys*., 2018, **20**, 14211.

[20] A. I. Krylov, *J. Chem. Phys.*, 2020, **153**, 080901.

[21] A. E. Reed, F. Weinhold, *J. Chem. Phys*., 1983, **78**, 4066.

[22] E. D. Glendening, C. R. Landis, F.Weinhold, *WIREs Comput. Mol. Sci.*, 2012, **2**, 1.

[23] A. Morita and S. Kato, *J. Am. Chem. Soc.*, 1997, **119**, 4021.

[24] R. McWeeny, *Rev. Mod. Phys.*, 1960, **32**, 335.

[25] J. Gerratt and I. M. Mills, *J. Chem. Phys*., 1968, **49**, 1719.

[26] J. A. Pople, R. Krishnan, H. B. Schlegel, and J. S. Binkley, *Int. J. Quantum Chem*., 1979, **16**, 225.

[27] M. Frisch, M. Head-Gordon, and J. Pople, *Chem. Phys*., 1990, **141**, 189.

[28] R. Fournier, *J. Chem. Phys*., 1990, **92**, 5422.

[29] R. L. Martin, *J. Chem. Phys*., 2003, **118**, 4775.

[30] J.-X. Zhang, F. K. Sheong, and Z. Lin, *Chem. - A Eur. J.*, 2018, **24**, 9639.

[31] F. K. Sheong, J.-X. Zhang, and Z. Lin, *Phys. Chem. Chem. Phys.*, 2020, **22**, 10076.

[32] J. Zhang, F. K. Sheong, and Z. Lin, *WIREs Comput. Mol. Sci.*, 2020, **10**, e1469.

[33] L. Eberson and S. S. Shaik, *J. Am. Chem. Soc.*, 1990, **112**, 4484.

[34] G. N. Sastry and S. Shaik, *J. Am. Chem. Soc*., 1995, **117**, 3290.

[35] G. N. Sastry and S. Shaik, *J. Phys. Chem.*, 1996, **100**, 12241.

[36] S. Shaik, D. Danovich, G. N. Sastry, P. Y. Ayala, and H. B. Schlegel, *J. Am. Chem. Soc.*, 1997, **119**, 9237.

[37] Y. Harabuchi and T. Taketsugu, *Theor. Chem. Acc.*, 2011, **130**, 305.

[38] Y. Alexeev, M. W. Schmidt, T. L. Windus, and M. S. Gordon, *J. Comput. Chem.*, 2007, **28**, 1685.

[39] M. Kohout, *Int. J. Quant. Chem.*, 2004, **97**, 651.

[40] M. Kohout, K. Pernal, F. R. Wagner, and Y. Grin, *Theor. Chem. Acc.*, 2004, **112**, 453.

[41] K. Fukui, *J. Phys. Chem.*, 1970, **74**, 4161.

[42] W. J. Hehre, R. Ditchfield, and J. A. Pople, *J. Chem. Phys.*, 1972, **56**, 2257.

[43] G. A. Petersson, A. Bennett, T. G. Tensfeldt, M. A. Al‐Laham, W. A. Shirley, and J. Mantzaris, *J. Chem. Phys.*, 1988, **89**, 2193.

[44] G. A. Petersson and M. A. Al‐Laham, *J. Chem. Phys.*, 1991, **94**, 6081.

[45] T. Clark, J. Chandrasekhar, G. W. Spitznagel, and P. V. R. Schleyer, *J. Comput. Chem*., 1983, **4**, 294.

[46] M.J. Frisch, G.W. Trucks, H.B. Schlegel, G.E. Scuseria, M.A. Robb, J.R. Cheeseman, G. Scalmani, V. Barone, G.A. Petersson, H. Nakatsuji, X. Li, M. Caricato, A. V Marenich, J. Bloino, B.G. Janesko, R. Gomperts, B. Mennucci, H.P. Hratchian, J. V Ortiz, A.F. Izmaylov, J.L. Sonnenberg, D. Williams-Young, F. Ding, F. Lipparini, F. Egidi, J. Goings, B. Peng, A. Petrone, T. Henderson, D. Ranasinghe, V.G. Zakrzewski, J. Gao, N. Rega, G. Zheng, W. Liang, M. Hada, M. Ehara, K. Toyota, R. Fukuda, J. Hasegawa, M. Ishida, T. Nakajima, Y. Honda, O. Kitao, H. Nakai, T. Vreven, K. Throssell, J. Montgomery, J. A., J.E. Peralta, F. Ogliaro, M.J. Bearpark, J.J. Heyd, E.N. Brothers, K.N. Kudin, V.N. Staroverov, T.A. Keith, R. Kobayashi, J. Normand, K. Raghavachari, A.P. Rendell, J.C. Burant, S.S. Iyengar, J. Tomasi, M. Cossi, J.M. Millam, M. Klene, C. Adamo, R. Cammi, J.W. Ochterski, R.L. Martin,

K. Morokuma, O. Farkas, J.B. Foresman, and D.J. Fox, Gaussian 16 (Revision C.01), Gaussian Inc., Wallingford, CT, 2016.

[47] T. H. Dunning, *J. Chem. Phys.*, 1989, **90**, 1007.

[48] R. A. Kendall, T. H. Dunning, and R. J. Harrison, *J. Chem. Phys.*, 1992, **96**, 6796.

[49] D. E. Woon and T. H. Dunning, *J. Chem. Phys*., 1993, **98**, 1358.

[50] X. Krokidis, S. Noury, and B. Silvi, *J. Phys. Chem. A*, 1997, **101**, 7277.

[51] A. D. Becke, and K. E. Edgecombe, *J. Chme. Phys.*, 1990, **92**, 5397.

[52] X. Krokidis, V. Goncalves, A. Savin, and B. Salvi, *J. Phys. Chem. A*, 1998, **102**, 5065.

[53] R. B. Campos and D. J. Tantillo, *Chem.*, 2019, **5**, 227.

[54] D. H. Nouri and D. J. Tantillo, *J. Org. Chem.*, 2006, **71**, 3686.

[55] D. J. Tantillo, *J. Phys. Org. Chem.*, 2008, **21**, 561.

[56] E. Anderson, Z. Bai, C. Bischof, S. Blackford, J. Demmel, J. Donngarra, J. Du Croz, A. Greenbaum,S. Hammerling, A. McKenney, and D. Sorenson, *LAPACK Users'Guide, 3rd edn.*, Society for Industrial and Applied Mathematics, Philadelphia, 1999.

[57] R. Dennington, T. A. Keith, and J. M. Millam, GaussView (Version 6.1), Semichem Inc., Shawnee Mission, KS, 2016.